Colloids and Surfaces A: Physicochemical and Engineering Aspects 674 (2023) 131912

Contents lists available at ScienceDirect

Colloids and Surfaces A: Physicochemical and Engineering Aspects

journal homepage: www.elsevier.com/locate/colsurfa

$Bi_2O_3/Bi_2O_{2.33}$@ECNF: A recyclable material for efficient adsorption and photocatalytic degradation of organic contaminants

Sheng-Zhe Zhao [a], Yi Yang [a], Ran Lu [a], Yan Wang [a], Hong-Lan Huang [a], Yong-Da Hu [b], Raul D. Rodriguez [c], Jin-Ju Chen [a,*]

[a] School of Materials and Energy, University of Electronic Science and Technology of China, Chengdu 610054, PR China
[b] School of Integrated Circuit Science and Engineering, University of Electronic Science and Technology of China, Chengdu 610054, PR China
[c] Tomsk Polytechnic University, 30 Lenin Ave, 634050, Tomsk, Russia

GRAPHICAL ABSTRACT

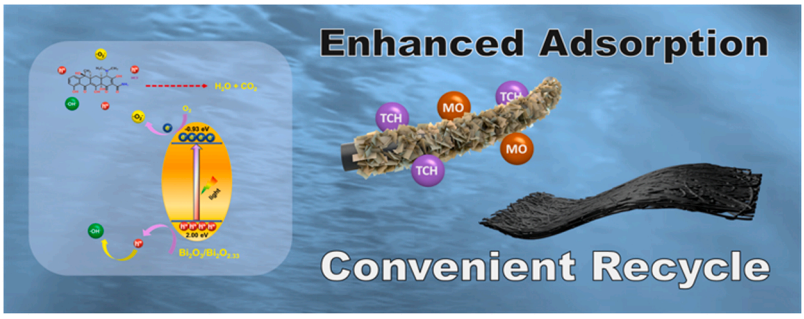

ARTICLE INFO

Keywords:
Bi_2O_3-$Bi_2O_{2.33}$
Adsorption
Convenient recycling
Photocatalysts
Water treatment

ABSTRACT

The removal of organic contaminants from water poses a significant challenge that can be tackled by integrating adsorption and photocatalytic degradation functions in a single architecture. However, traditional powdery nanomaterials face challenges in separation and lack synergistic function, hampering their practical application. This study presents a one-step hydrothermal synthesis of a convenient recyclable $Bi_2O_{2.33}/Bi_2O_3$@ECNF (electrospun carbon nanofibers), which combines both adsorption and photocatalytic performance. The $Bi_2O_{2.33}/Bi_2O_3$ exhibits high adsorption removal of methyl orange (MO), reaching 94.56 % and a maximum capacity of 213.13 mg g^{-1}. Additionally, the $Bi_2O_{2.33}/Bi_2O_3$ shows a high charge transfer rate, strong redox ability, and efficient removal of Rhodamine B (RhB) at 83.01 %. Loading the $Bi_2O_{2.33}/Bi_2O_3$ on lightweight carbon fibers allows for easy recycling. The $Bi_2O_{2.33}/Bi_2O_3$@ECNF demonstrates excellent stability and reusability, with a removal rate of 87.37 % for tetracycline hydrochloride (TCH) at high concentrations. This work presents a promising solution for the practical application of photocatalysts by overcoming the limitations of single photocatalysts and minimizing secondary pollution from single adsorbents.

* Corresponding author.
E-mail address: jinjuchen@uestc.edu.cn (J.-J. Chen).

https://doi.org/10.1016/j.colsurfa.2023.131912
Received 5 February 2023; Received in revised form 14 June 2023; Accepted 19 June 2023
Available online 20 June 2023

1. Introduction

The fast pace of industrialization in recent decades has brought about economic prosperity, but it has also led to increased wastewater pollution. The main factors causing environmental pollution are organic dyes [1] and antibiotics [2] extensively used in industries and medicine. Synthetic organic dyes, such as methyl orange (MO), congo red (CR), and rhodamine B (RhB), not only strongly stimulate to the skin and mucous membranes but also have a carcinogenic and mutagenic properties [3], which can harm aquatic organisms and humans. Antibiotics, such as tetracycline hydrochloride (TCH), are commonly used to treat humans and animals for infectious diseases. Discharging wastewater that contains these residues into the environment can result in drinking water risks, enhance bacterial drug resistance, and disrupt the ecological balance [4]. Moreover, the aromatic structure of these organic pollutants confers on them physicochemical, thermal and optical stability, making them difficult to degrade naturally [5]. Therefore, it is of environmental significance to remove these pollutants from wastewater before they are discharged [6,7].

The purification of contaminated water has been explored through various approaches such as adsorption [8], photodegradation [9–12], advanced oxidation [13], electrochemical oxidation [14,15], biodegradation [16], membrane distillation [17] and filtration [18]. While adsorption is the most widely used due to its low cost, fast speed, and ease of operation [19], it can result in secondary pollution during the adsorbent's regeneration process [20]. On the other hand, photocatalytic degradation is deemed to be a green and effective approach, but it faces limitations in reaction kinetics and separation costs for removing pollutants in wastewater [21]. A combination of adsorption and photocatalysis is an encouraging approach for organic pollutant purification [22–25]. This method addresses the slow kinetics of a single photocatalyst and eliminates the secondary pollution caused by a single adsorbent.

There has been extensive research on treating organic pollutants using combined adsorption and degradation methods [26–30]. For instance, Tian et al. [20] synthesized a g-C_3N_4 thin nanosheets (CNNS) photocatalyst that demonstrated a maximum adsorption capacity of 89 mg g^{-1} for TCH, with a removal rate of over 75 % after 1 h degradation. Su et al. [24] used a simple one-step gelation-pyrolysis route to obtain N-doped carbon/CuO bulky composites that exhibited a maximum adsorption capacity for TCH of 25.03 mg g^{-1}, and could remove over 90 % of TCH in 240 min. It is evident from these studies that insufficient adsorption capacity significantly limits the removal rate of high-concentration pollutants. Bismuth oxide has been extensively studied as a pure photocatalyst with high photocatalytic degradation ability [31], [32]. Interestingly, non-stoichiometric $Bi_2O_{2.33}$ has good adsorption properties, and flower-like $Bi_2O_{2.33}$ exhibits high adsorption capacities of 285 and 229 mg g^{-1} for I^- and IO_3^- [33]. Therefore, it is valuable to prepare a photocatalyst that combines the high adsorption capacity of $Bi_2O_{2.33}$ with the excellent photocatalytic properties of Bi_2O_3.

Herein, $Bi_2O_{2.33}/Bi_2O_3$ was prepared to integrate adsorption and photocatalytic performance. It exhibited a rapid adsorption rate of 94.56 % for MO within 20 min, a maximum adsorption capacity of 213.13 mg g^{-1}, and a high removal rate of 83.01 % for RhB after photocatalytic degradation. By integrating adsorption and photodegradation, high-concentration TCH was efficiently removed by 87.37 %. The adsorption kinetics, isothermal adsorption model, degradation kinetics, and photodegradation mechanism for organic pollutants molecules over the $Bi_2O_{2.33}/Bi_2O_3$ were systematically investigated. Furthermore, the $Bi_2O_{2.33}/Bi_2O_3$ was loaded onto electrospun carbon nanofibers (ECNF) via a one-step hydrothermal method to obtain $Bi_2O_{2.33}/Bi_2O_3$@ECNF catalysts, which can be easily recycled and reused, and exhibit fine performance for organic contaminants eliminating and good cyclic degradation stability.

2. Experimental

2.1. Materials

Bismuth nitrate pentahydrate ($Bi(NO_3)_3{\cdot}5H_2O$) was purchased from Aladdin Reagent Co., Ltd. (Shanghai, China). Ethanol anhydrous (EA), RhB and MO were obtained from Jinshan Chemical Reagent Co., Ltd. (Chengdu, China). Congo red (CR), malachite green (MG), eosin y (EY), methylene blue (MB), and fuchsin were purchased from Shanghai D&B Biotechnology Science and Technology Co., Ltd. (Shanghai, China). Ethylene glycol (EG) and TCH were supplied by Shanghai Macklin Biochemical Co., Ltd. (Shanghai, China). Ethylenediaminetetraacetic acid disodium salt (EDTA-2Na), benzoquinone (BQ), and t-butanol (TBA) were supplied by Chengdu Chron Chemicals Co., Ltd (Chengdu, China). All chemicals were of analytical reagent grade and used without further purification.

2.2. Preparation of $Bi_2O_3/Bi_2O_{2.33}$ and $Bi_2O_3/Bi_2O_{2.33}$@ECNF

In a typical procedure, 1.516 g of $Bi(NO_3)_3{\cdot}5H_2O$ was dissolved in 25 mL of EG, and stirred in a water bath at a temperature of 60 °C for 30 min until the solute was completely dissolved to obtain a precursor solution. 8 mL of precursor solution and 16 mL of EA were charged into a 50 mL Teflon-lined autoclave. Subsequently, the autoclave was put into an electric oven and kept at 160 °C for 5 h. Then the autoclave was naturally cooled to room temperature. Finally, the obtained $Bi_2O_3/Bi_2O_{2.33}$ were collected and washed with ethanol and deionized water several times to remove any ionic residue and then dried in an oven at 60 ºC for 6 h. For comparison, pure-phase Bi_2O_3 was obtained after $Bi_2O_3/Bi_2O_{2.33}$ was annealed at 450 ºC for 1 h. The $Bi_2O_3/Bi_2O_{2.33}$@ECNF was obtained by adding ECNF (1 cm * 1.5 cm) into the autoclave while other conditions were kept unchanged.

2.3. Characterization

The morphologies of the samples were obtained by the scanning electron microscopic (SEM, Thermo Fisher Scientific, USA) and transmission electron microscopy (TEM, Tecnai G2, operating voltage: 15 kV). The crystal structures of samples were examined using X-ray powder diffraction (XRD) on an Empyrean X-ray diffractometer (PANalytical B.V, Netherlands). X-ray photoelectron spectra (XPS) were recorded using an AXIS Supra X-ray electron spectrometer (Kratos, UK). The UV-Vis diffuse reflectance spectra (DRS) were measured using a PerkinElmer Lambda 1050 +. Photoluminescence (PL) spectra were recorded on an F-7000 fluorescence spectrophotometer (Hitachi, Japan) with an excitation wavelength of 350 nm.

2.4. Adsorption experiments

Four anionic dyes (MO, CR, MG, EY), three cationic dyes (RhB, MB, Fuchsin), and TCH were used to evaluate the adsorption behavior of $Bi_2O_3/Bi_2O_{2.33}$. Typically, 25 mg of $Bi_2O_3/Bi_2O_{2.33}$ was dispersed in 25 mL MO solution with different concentrations under mild stirring at 25 °C. 500 μL of the dispersion was taken out via filtrating by 0.22 μm PTFE syringe filters and then diluted to 4 mL to measure absorbance with a UV-Vis spectrometer at given time intervals. The adsorption capacities of the $Bi_2O_3/Bi_2O_{2.33}$ were calculated according to the following Eq. (1):

$$q_t = \frac{(C_0 - C_t)V}{m} \quad (1)$$

where q_t is the adsorption capacity (mg g^{-1}) at t min, C_0 and C_t are the concentrations of the adsorbate (mg L^{-1}) at 0 and t min respectively, V is the volume of the solution (mL), and m is the mass of the adsorbent (g).

2.5. Photocatalytic evaluation

The samples' photocatalytic activities were evaluated by the degradation of RhB and TCH. 25 mg catalyst was mixed with 25 mL RhB (10 mg L^{-1}) to obtain a suspension, which was magnetically stirred in the dark for 1.5 h to ensure adsorption equilibrium. Then, the suspension was irradiated under a Xenon lamp (300 W) for photocatalytic degradation. At certain time intervals, 2 mL dispersion was collected from the reaction cell via filtrating by 0.22 μm PTFE syringe filter to remove the catalyst powders. Then, the obtained solution was loaded in a UV-Vis spectrophotometer. The degradation efficiency of RhB was analyzed by comparing the characteristic absorption intensity at 560 nm at different times with that of the original RhB solution. For TCH degradation, the initial concentration of TCH solution was 50 mg L^{-1}, and the characteristic absorption peak was monitored at 357 nm.

3. Results and discussion

Fig. 1a and 1b show the SEM images of the as-prepared samples. The pore-like microstructure, formed by agglomeration of a mass of $Bi_2O_{2.33}/Bi_2O_3$ nanosheets, providing a large specific surface area, is beneficial for the adsorption and photocatalytic degradation of organic contaminants. As shown in Fig. S1, the original porous structure disappeared for the sample after annealing. The XRD patterns are shown in Fig. 1c. For the as-prepared sample before annealing, the diffraction peaks at 10.2° and 20.5° can be ascribed to the (004) and (008) planes of the body-centered tetragonal $Bi_2O_{2.33}$ (JCPDS No. 27–0051), respectively. However, the theoretical maximum diffraction peak corresponding to the (107) plane of $Bi_2O_{2.33}$ is not found in the XRD pattern. This peak's absence may be caused by the preferential growth of the {001} [33,34]. The diffraction peak of the tetragonal β-Bi_2O_3 (JCPDS No. 27–0050) can also be found in this spectrum. The peaks at 27.91°, 31.03°, and 32.71° are attributed to the (201), (002), and (220) planes, respectively. The diffraction peaks for the sample obtained after annealing are consistent with those of the tetragonal β-Bi_2O_3. The main peaks at 27.89°, 31.65°, 32.70°, 46.17°, 46.93°, 54.10°, 55.52°, and 57.67° are attributed to (201), (002), (220), (222), (400), (203), (421), and (402) planes, respectively. The disappearance of $Bi_2O_{2.33}$ indicates that the oxygen vacancies in $Bi_2O_{2.33}$ are occupied by oxygen in the air during annealing treatment.

To further observe the microstructure of $Bi_2O_{2.33}/Bi_2O_3$, the TEM of the $Bi_2O_{2.33}/Bi_2O_3$ was performed as shown in Fig. 1e. Similar to the results of SEM, the sample exhibits a classical nanosheet structure. The high-resolution transmission electron microscopy (HRTEM) of $Bi_2O_{2.33}/Bi_2O_3$ nanosheets are shown in Fig. 1d and 1f. Obviously, the lattice fringes of the nanosheet are relatively homogeneous (Fig. 1d), which exhibits the lattice spacing of 0.317 nm indexing to the (201) crystal planes of Bi_2O_3. As shown in Fig. 1f, the lattice spacing of about

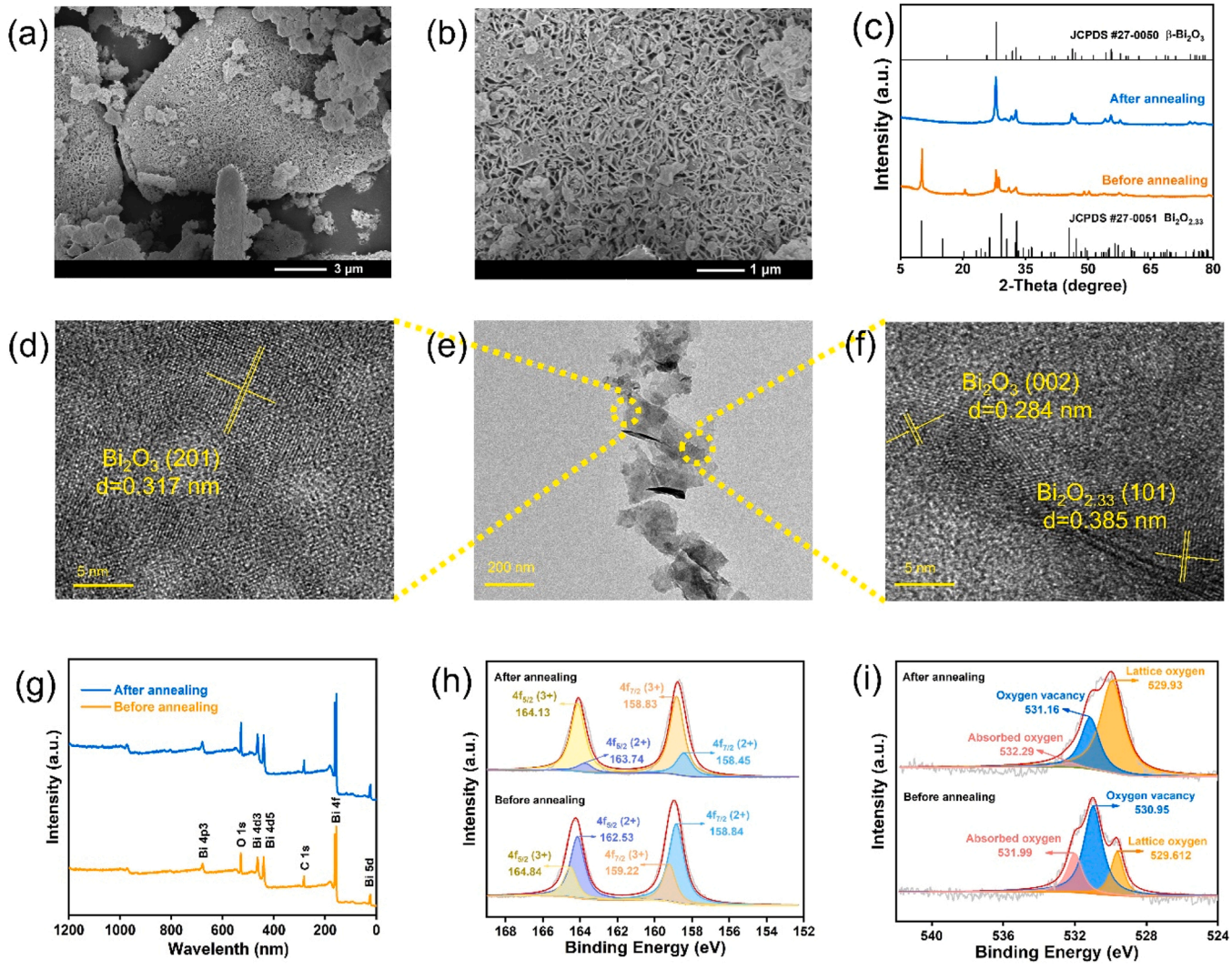

Fig. 1. SEM (a-b) images, XRD (c) surveys, TEM (e) and HRTEM (d,f) images of $Bi_2O_3/Bi_2O_{2.33}$. XPS (g) surveys, high-resolution Bi 4f (h) XPS spectra, and high-resolution O 1s (i) XPS spectra of samples before and after annealing.

0.284 nm and 0.385 nm corresponds to Bi_2O_3 (002) and $Bi_2O_{2.33}$ (101) crystal planes respectively, indicating the existence of $Bi_2O_{2.33}$ and Bi_2O_3.

To investigate the chemical state of elements, XPS measurement was performed. In Fig. 1g, the XPS survey spectra of samples show the typical Bi 4f and O 1s peaks. The peak at the binding energy of 980.00 eV is attributed to the O KLL Auger peak [35]. Fig. 1h shows the high-resolution Bi 4f XPS spectra of samples before and after annealing. For the sample before annealing, the main peaks at 162.53 eV and 158.84 eV are ascribed to Bi $4f_{5/2}$ and Bi $4f_{7/2}$ of Bi^{2+}, and the peaks at 164.84 eV and 159.22 eV are ascribed to Bi $4f_{5/2}$ and Bi $4f_{7/2}$ of Bi^{3+}, respectively. [36–38] For the sample after annealing, Bi^{3+} $4f_{5/2}$ and $4f_{7/2}$ peaks are located at 164.13 eV and 158.83 eV, respectively, and peaks at 163.74 eV and 158.45 eV belong to Bi^{2+} $4f_{5/2}$ and $4f_{7/2}$. Annealing leads to a drastic decrease in the Bi^{2+} 4f peaks intensity and a significant increase of Bi^{3+} 4f peaks, indicating a substantial conversion of $Bi_2O_{2.33}$ into Bi_2O_3. As shown in Fig. 1i, the O 1s spectra can be deconvoluted into three peaks: the lattice oxygen (O_L) in metal oxide (Bi-O), the oxygen vacancy (O_V) in the lattice [39,40], and the surface chemisorbed oxygen (Oc) such as O in H_2O [36,41]. The ratio of O_V to O_L can be calculated to estimate the relative amount of oxygen vacancies [42,43], which is 4.13 and 0.441 for the sample before and after annealing, respectively, suggesting that the amount of oxygen vacancies decreases greatly after annealing. In conclusion, the results of XPS show the existence of Bi^{2+} and oxygen vacancies to demonstrate further that the sample before annealing abounds with $Bi_2O_{2.33}$, which is consistent with the XRD result.

$Bi_2O_3/Bi_2O_{2.33}$ was used to adsorb different dye solutions of 400 mg L^{-1} at 25 ℃ to test its adsorption performance. As shown in Fig. 2a, the equilibrium adsorption capacity of $Bi_2O_{2.33}/Bi_2O_3$ for CR, MG, MO, EY, RhB, MB, and fuchsin is 397, 383, 224, 220, 51, 50, and 24 mg g^{-1}, respectively. It can be found that the sample exhibits remarkable adsorption performance for anionic dyes, which may be due to the positive surface charge caused by the oxygen vacancy of $Bi_2O_{2.33}$. To confirm that this effect does come from adsorption rather than other reactions, a mixed solution of 100 mg L^{-1} MO and 100 mg L^{-1} RhB was treated with $Bi_2O_3/Bi_2O_{2.33}$ and the UV-Vis spectra were investigated (Fig. S2 in Supporting Information). Obviously, after 10 min of adsorption, the characteristic peak of anionic dye MO at 464 nm almost disappears, while the intensity of the characteristic peak of cationic dye RhB at 560 nm decreases only slightly. In summary, it can be determined that this is a pure adsorption process that is selective to anionic dyes.

The pH level of practical sewages can vary, affecting the adsorption process. To explore this effect, the $Bi_2O_3/Bi_2O_{2.33}$ material was tested for its ability to adsorb MO (100 mg L^{-1}) under different pH at 25 ℃. Fig. 2b shows that the adsorption capacity of the $Bi_2O_3/Bi_2O_{2.33}$ to MO is strong in acidic and near-neutral conditions. In alkaline conditions, the adsorption capacity decreases rapidly, which is less than half of the former. The adsorption ability of the $Bi_2O_3/Bi_2O_{2.33}$ for dyes is mainly from the van der Waals force between the electropositive surface of the sample and the anions in the dye solution (discussed in detail in the following mechanism section). Many OH^- anions in an alkaline solution can also be adsorbed to the samples' surface due to the Coulomb force. This results in the competition for adsorption sites between dye anions and hydroxide ions, thus leading to the loss of adsorption capacity. The change in temperature will also have an effect on the adsorption of dyes. The adsorption capacity of $Bi_2O_{2.33}/Bi_2O_3$ for MO dyes (100 mg L^{-1}) with respect to temperature and time variation is shown in Fig. 2c. It is clear that higher temperature results in faster adsorption and larger adsorption capacity, which may be caused by the acceleration of molecular thermal motion.

To further figure out the adsorption behavior of $Bi_2O_{2.33}/Bi_2O_3$ to anionic dyes, MO was still selected as a representative anionic dye for adsorption experiments. Fig. 2d shows the adsorption of $Bi_2O_3/Bi_2O_{2.33}$ for MO with different initial concentrations. It is obvious that initial MO concentration plays an essential role in the adsorption process, and the adsorption capacity increases with the initial solution concentration. After 120 min adsorption, it is 48.75, 92.91, and 118.86 mg g^{-1} for the MO initial concentration of 50, 100, and 150 mg L^{-1}, respectively. Almost all of the MO are removed when the initial concentration is relatively low, which is considered significant in industrial applications since the concentration of practical sewage is about 10–60 mg L^{-1} [6,

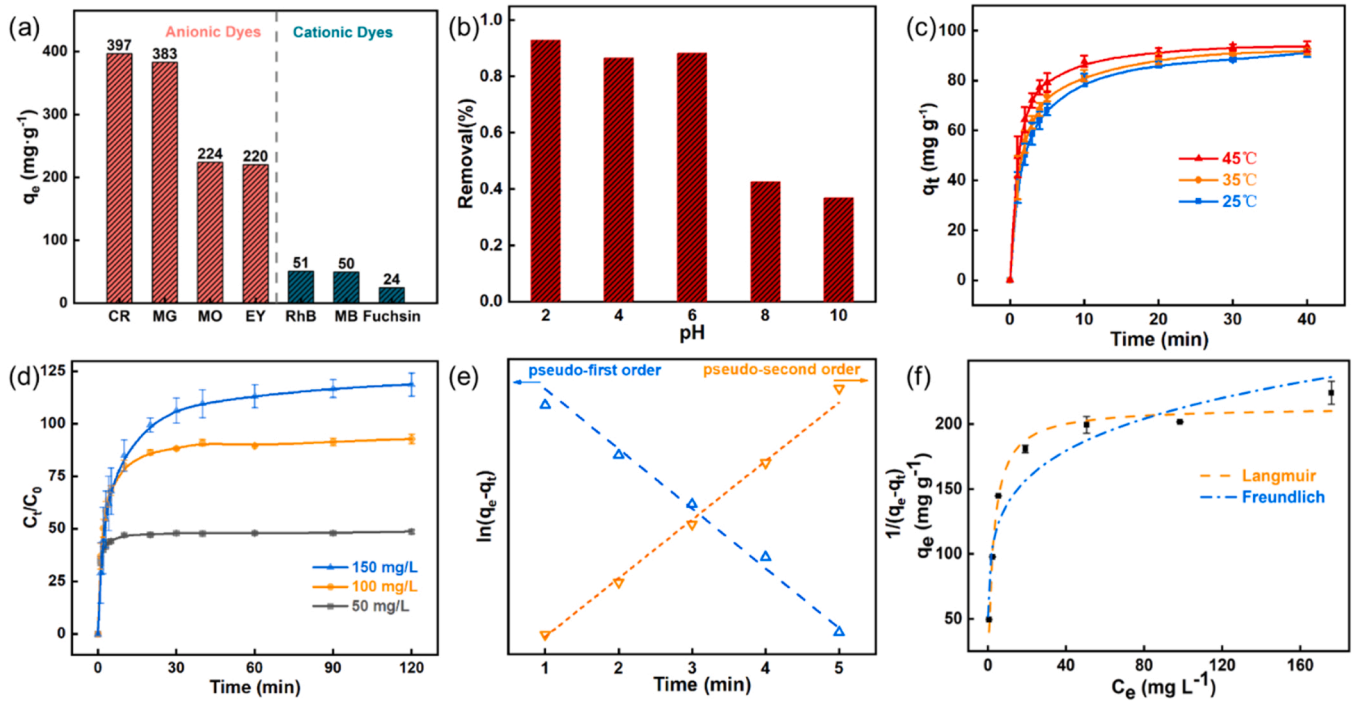

Fig. 2. (a) The equilibrium adsorption capacity of $Bi_2O_3/Bi_2O_{2.33}$ for different dye solutions (C_0 = 400 mg L^{-1}), (b) The removal rate of 100 mg L^{-1} MO at different pH, (c) Adsorption kinetic curves of 100 mg L^{-1} MO over $Bi_2O_3/Bi_2O_{2.33}$ at different temperature, (d) Adsorption kinetic curves of MO with different initial concentration, (e) Fitting results of pseudo-first order and pseudo-first order model, and (f) Adsorption isotherms of MO by Langmuir and Freundlich models.

44]. The sample has rapid adsorption kinetics. The 50 mg L^{-1} MO takes only 20 min to approach the adsorption equilibrium, and the adsorption rate reaches 94.56 %.

To further study the adsorption kinetics of the $Bi_2O_3/Bi_2O_{2.33}$, pseudo-first-order and pseudo-second-order models are used to fit the experimental data (see more description in Supporting Information). The two models differ in the assumed adsorption rate control steps. The pseudo-first-order model assumes the internal diffusion process as the rate-controlling step, while the pseudo-second-order model assumes the adsorption of molecules on active sites as the rate-controlling step. The fitting results of the adsorption for 100 mg L^{-1} MO using these two kinetic models are presented in Fig. 2e. More fitting results and details are shown in Table S1 and Fig. S3. Comparing these results, it is not difficult to find that the fitting correlation coefficient of the pseudo-second-order model is larger than that of the pseudo-first-order model. The adsorption process of MO is mainly ruled by the interaction between ionized pollutant molecules and active sites of the $Bi_2O_3/Bi_2O_{2.33}$, illustrating that the internal diffusion process of adsorption is fast. The capillary effect from the porous structure formed by bismuth oxide nanosheets may greatly accelerate the internal diffusion process.

The adsorption behavior of the samples was quantitatively analyzed by Langmuir isothermal adsorption model and the Freundlich isotherm adsorption model (see more description in Supporting Information). The Langmuir isotherm adsorption model assumes that the adsorption occurs on a uniform surface with a homogeneous active site through monolayer adsorption. Therefore, adsorption can reach saturation. The Freundlich isothermal adsorption model assumes that multi-layer adsorption occurs on heterogeneous surfaces. The fitting results of isothermal adsorption models are shown in Fig. 2f. It can be seen that the Langmuir model has a better correlation (correlation coefficient R^2 = 0.985) with the experimental data than the Freundlich model (R^2 = 0.892), indicating that the adsorption of MO on the $Bi_2O_3/Bi_2O_{2.33}$ surface is monolayer adsorption with a maximum adsorption capacity of 213.13 mg g^{-1}.

Photodegradation of RhB and TCH has been carried out to investigate the photocatalytic activity of the $Bi_2O_3/Bi_2O_{2.33}$. Since the synthesized $Bi_2O_3/Bi_2O_{2.33}$ is mainly used for selective adsorption of anionic dyes, choosing RhB to simulate organic pollutants is helpful to eliminate the interference of adsorption and better study the photocatalytic performance of the $Bi_2O_3/Bi_2O_{2.33}$ material. As a kind of antibiotic pollutant that exists widely in water, the degradation of TCH has more practical significance. Therefore, TCH is also chosen as an organic pollutant to be degraded. As shown in Fig. 3a, the $Bi_2O_3/Bi_2O_{2.33}$ shows good photocatalytic activity to RhB. After 180 min of degradation, the removal rate of RhB reaches 83.01 %. Fig. 3b demonstrates the ability of the $Bi_2O_3/Bi_2O_{2.33}$ to efficiently treat high-concentration TCH solution of 50 mg L^{-1} through the combination of adsorption and degradation. After rapid physical adsorption, more than 74.6 % of the TCH is quickly removed. And then, after 180 min of degradation, the removal rate of TCH reached 87.37 %.

Zero-order and first-order kinetics were used to study the kinetics of the photocatalytic degradation process. In zero-order kinetics, the degradation rate is a constant, described by Eqs. (2) and (3):

$$-\frac{dC}{dt} = k_0 \tag{2}$$

$$\frac{C}{C_0} = -\left(\frac{k_0}{C_0}\right)t + \frac{C_0'}{C_0} \tag{3}$$

where k_0 (mg L^{-1} min^{-1}) is the zero-order kinetic rate constant, and C_t (mg L^{-1}) and C_0' (mg L^{-1}) are the concentration of organic pollutes in the reaction solution at time t and initial time of photocatalysis, respectively.

In the first-order kinetics, the degradation rate is proportional to the solution concentration, and its equation is shown in formulas (4) and (5):

$$-\frac{dC}{dt} = k_1 C \tag{4}$$

$$\ln\left(\frac{C}{C_0'}\right) = -k_1 t \tag{5}$$

where k_1 (min^{-1}) is the first-order kinetic rate constant.

Interestingly, RhB and TCH degradation by $Bi_2O_3/Bi_2O_{2.33}$ exhibits

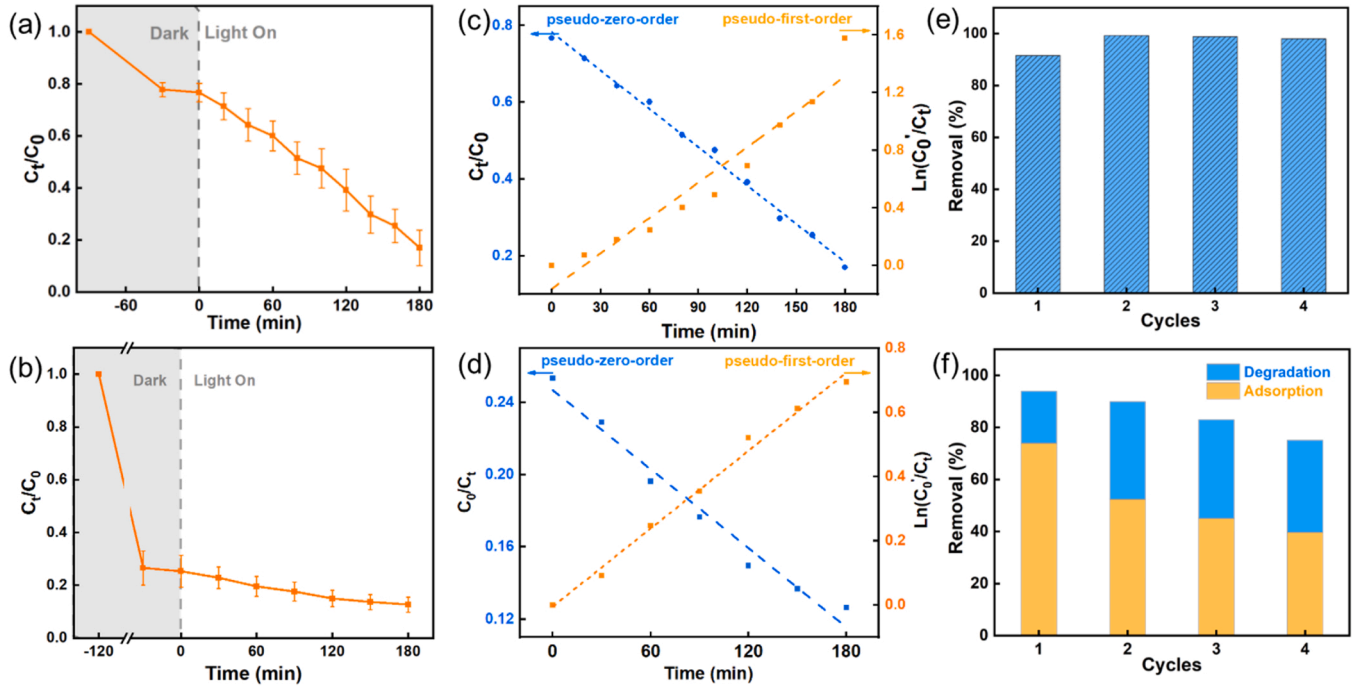

Fig. 3. Degradation curve of (a) 10 mg L^{-1} RhB and (b) 50 mg L^{-1} TCH over $Bi_2O_3/Bi_2O_{2.33}$, kinetic linear simulation of (c) 10 mg L^{-1} RhB and (d) 50 mg L^{-1} TCH over $Bi_2O_3/Bi_2O_{2.33}$, and photocatalytic degradation cycling test of (e) 10 mg L^{-1} RhB and (f) 50 mg L^{-1} TCH.

different kinetic characterization. As shown in Fig. 3c, the kinetic fitting results suggest that the photocatalytic degradation of RhB is close to the zero-order kinetic process. The degradation rate is a constant independent of solution concentration. The kinetic fitting results for the photocatalytic degradation of TCH are shown in Fig. 3d. The degradation process of TCH is more consistent with the first-order kinetic model. During the degradation, the concentration of TCH decreases gradually so that the adsorption sites of $Bi_2O_3/Bi_2O_{2.33}$ cannot be saturated, leading to a degradation rate decrease. It is evident that the degradation kinetics of RhB and TCH is closely related to their adsorption characteristics on $Bi_2O_3/Bi_2O_{2.33}$.

The reusability of $Bi_2O_3/Bi_2O_{2.33}$ for the photocatalytic degradation of 10 mg L^{-1} RhB and 50 mg L^{-1} TCH was explored. As shown in Fig. 3e, the photocatalytic performance of $Bi_2O_3/Bi_2O_{2.33}$ gets enhanced in the second cycle. This improvement in the photocatalytic performance is due to the increase of the specific surface area of $Bi_2O_3/Bi_2O_{2.33}$ caused by long-time stirring, which is demonstrated by the morphology change in Fig. S4. In the following three cycles of degradation, the removal rate of RhB is steady at about 97 %, showing excellent photocatalytic stability of $Bi_2O_3/Bi_2O_{2.33}$. Fig. 3f shows the cyclic photocatalytic degradation of TCH over $Bi_2O_3/Bi_2O_{2.33}$. The removal ratio of TCH tends to decrease slowly with the cycle. To figure out the reasons for this observation, the removal ratio is disassembled into adsorption and degradation contributions. Similarly, after the first cycle, the photocatalytic activity increases as the morphology changes. After that, the photocatalytic performance reached a stable state. The decrease in the overall removal rate is mainly due to the decline in adsorption performance. This may be caused by the fact that the photocatalytic process did not completely restore the adsorption active sites of $Bi_2O_{2.33}/Bi_2O_3$. As shown in Fig. S5, the XRD patterns indicate that the crystal structure of the $Bi_2O_{2.33}/Bi_2O_3$ remains unchanged before and after cycling tests. These results show that the stability of the photocatalytic performance of $Bi_2O_{2.33}/Bi_2O_3$ is satisfactory.

In practical applications, the powdery photocatalyst is difficult to separate directly from the liquid phase, which makes its recovery costly. To solve this problem, the photocatalyst was grown on a flexible ECNF (shown in Fig. S6) for convenient recycling and reusing. As shown in Fig. 4a, $Bi_2O_3/Bi_2O_{2.33}$ is stacked in sheets and grows uniformly on the surface of electrospun carbon fibers. This structure can provide a large surface area, which is beneficial for adsorption and photocatalysis. Using flexible ECNF as the substrate helps improve the structural reliability of materials and obtain good cycle stability. The EDX mapping in Fig. 4b proves that C, Bi, and O are uniformly present in $Bi_2O_3/Bi_2O_{2.33}$@ECNF. Fig. 4c shows the adsorption kinetics curve of the $Bi_2O_3/Bi_2O_{2.33}$@ECNF to 100 mg L^{-1} MO solution. The $Bi_2O_3/Bi_2O_{2.33}$@ECNF shows pretty good adsorption properties for MO. After 120 min of adsorption, the removal rate of MO is up to 96.11 %. The fitting results of the adsorption performance of $Bi_2O_3/Bi_2O_{2.33}$@ECNF using pseudo-first-order and pseudo-second-order kinetics models are shown in Fig. S7 and Table S2. The pseudo-first-order kinetics (R^2 =0.9925) has a higher correlation coefficient than the pseudo-second-order kinetics (R^2 =0.9908). This indicates that the adsorption of dye molecules on the adsorption sites is the controlling step of the entire process, which is consistent with the adsorption kinetic characteristics of $Bi_2O_3/Bi_2O_{2.33}$. It suggests that $Bi_2O_3/Bi_2O_{2.33}$@ECNF exhibits similar kinetic characteristics to $Bi_2O_3/Bi_2O_{2.33}$ and also possesses excellent adsorption performance. The adsorption rate of the $Bi_2O_3/Bi_2O_{2.33}$@-ECNF to MO is slower than that of the powdery $Bi_2O_3/Bi_2O_{2.33}$, which is caused by the decrease of the dispersibility of adsorbent in solution after being loaded on the carbon fiber substrate. Moreover, the photocatalytic activity of $Bi_2O_3/Bi_2O_{2.33}$@ECNF is also good. Fig. 4d shows the photocatalytic degradation of 50 mg L^{-1} TCH by the $Bi_2O_3/Bi_2O_{2.33}$@ECNF. After two hours of stirring in the dark, 54.9 % of TCH is removed by adsorption. Then, after six hours of photocatalytic degradation, the removal rate of TCH reaches 85 %. The cyclic photocatalytic degradation of 50 mg L^{-1} TCH was also carried out to explore the cyclic stability of the $Bi_2O_3/Bi_2O_{2.33}$@ECNF. As shown in Fig. 4e, the adsorption capacity decreases obviously after the first cycle and then tends to be stable, which is consistent with the powdery $Bi_2O_3/Bi_2O_{2.33}$. Although the combination of $Bi_2O_3/Bi_2O_{2.33}$ and ECNF leads to a slight decrease in the kinetic rate of both adsorption and degradation, the $Bi_2O_3/Bi_2O_{2.33}$@ECNF is greatly convenient for recycling and stable, which

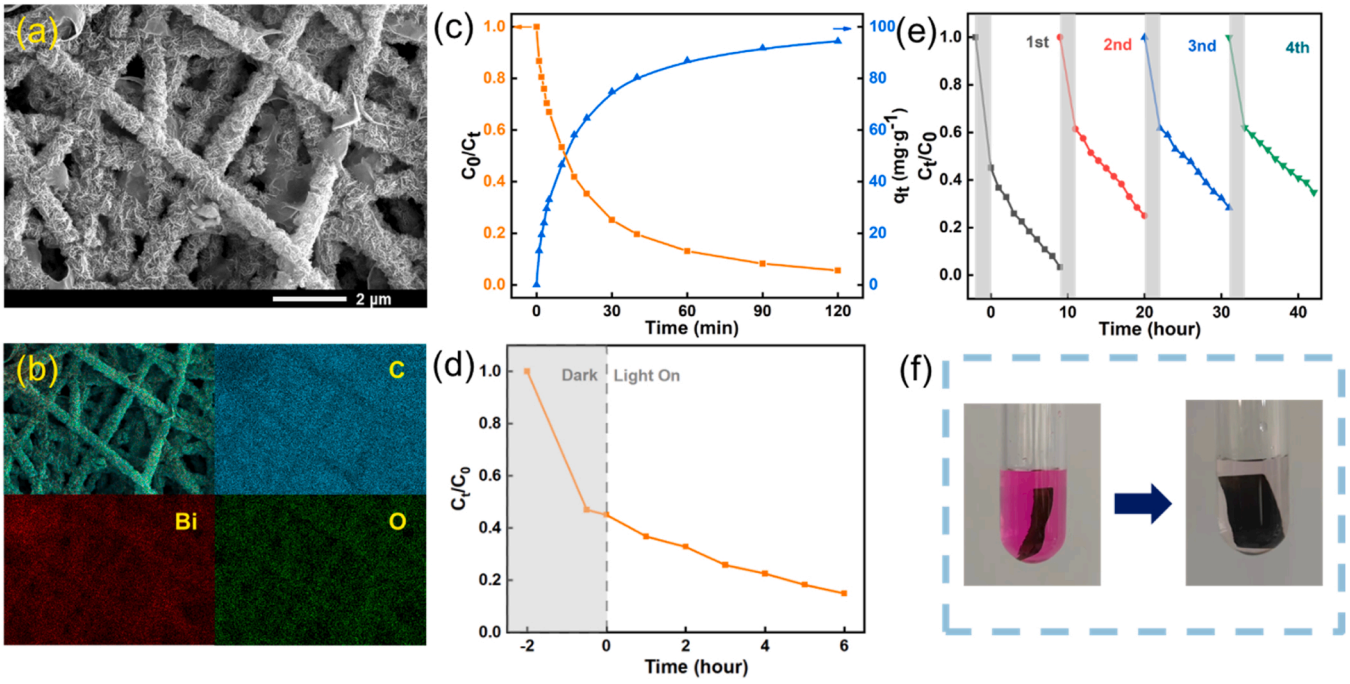

Fig. 4. (a) SEM images of $Bi_2O_3/Bi_2O_{2.33}$@ECNF, (b) EDX mapping of $Bi_2O_3/Bi_2O_{2.33}$@ECNF, (c) Adsorption kinetic curve of 100 mg L^{-1} MO solution with $Bi_2O_3/Bi_2O_{2.33}$@ECNF, (d) Degradation curve of 50 mg L^{-1} TCH with $Bi_2O_3/Bi_2O_{2.33}$@ECNF, (e) Photocatalytic degradation cycling test of 50 mg L^{-1} TCH with $Bi_2O_3/Bi_2O_{2.33}$@ECNF, and (f) images of RhB solution before and after photodegradation.

better meet the practical application requirements of pollutant elimination. Fig. 4f exhibits the color comparison of RhB solution before and after photocatalytic degradation by the $Bi_2O_3/Bi_2O_{2.33}$@ECNF. After degradation, RhB solution becomes almost colorless and transparent. It is clear that the $Bi_2O_3/Bi_2O_{2.33}$@ECNF can be easily recycled.

To investigate the role of non-stoichiometric $Bi_2O_{2.33}$ in the whole process of adsorption and degradation, the adsorption-degradation properties and optical properties of two kinds of bismuth oxide ($Bi_2O_{2.33}/Bi_2O_3$ and β-Bi_2O_3) were tested. β-Bi_2O_3 was obtained by annealing $Bi_2O_{2.33}/Bi_2O_3$. Fig. 5a shows the adsorption to MO (100 mg L^{-1}) using different bismuth oxides. β-Bi_2O_3 almost losses its adsorption capacity, indicating that the non-stoichiometric $Bi_2O_{2.33}$ is responsible for the adsorption of dyes. Due to the presence of oxygen vacancies, the sample shows a positive surface charge, which has a good adsorption effect on anionic dyes such as MO. Annealing in air causes oxygen atoms to enter the lattice of $Bi_2O_{2.33}$ to fill the oxygen vacancy, resulting in a sharp reduction in the number of positive charges, leading to a decrease in adsorption performance. Fig. 5b shows the photocatalytic degradation of RhB (10 mg L^{-1}) over the $Bi_2O_{2.33}/Bi_2O_3$ and the β-Bi_2O_3. It can be seen that the photocatalytic performance of the β-Bi_2O_3 decreases significantly. To explain the difference in the photocatalytic performance of samples $Bi_2O_{2.33}/Bi_2O_3$ and pure-phase Bi_2O_3, the optical and electrical properties of the two were investigated. Fig. 5c shows the electrochemical impedance spectra (EIS). Notably, the $Bi_2O_{2.33}/Bi_2O_3$ shows a smaller arc radius than the β-Bi_2O_3, which indicates lower charge-transfer resistance in the $Bi_2O_{2.33}/Bi_2O_3$ sample.

The samples' UV-Vis diffuse reflectance spectra (DRS) are shown in Fig. 5d. The β-Bi_2O_3 has a wider light absorption range than the $Bi_2O_{2.33}/Bi_2O_3$. The color of samples changes from off-white for the $Bi_2O_{2.33}/Bi_2O_3$ to yellow for the β-Bi_2O_3, which is consistent with DRS results (the β-Bi_2O_3 absorbs light with wavelength up to 500 nm, making the color yellow). As shown in Fig. 5e, the estimated optical bandgap energy (E_g) value of $Bi_2O_{2.33}/Bi_2O_3$ and β-Bi_2O_3 is approximately 2.93 eV and 2.15 eV, respectively. The $Bi_2O_{2.33}/Bi_2O_3$ bandgap is much larger than that of β-Bi_2O_3. The Mott-Schottky test was carried out to determine the relative positions of the conduction band (CB) and valence band (VB) edges. As seen in Fig. 5f, the flat band potentials (E_{fb}) of the $Bi_2O_3/Bi_2O_{2.33}$ and the β-Bi_2O_3 are 1.80 eV and 1.49 eV vs. NHE (Normal Hydrogen Electrode), respectively. The negative slope of Mott-Schottky curves indicates that the as-prepared $Bi_2O_3/Bi_2O_{2.33}$ and β-Bi_2O_3 are typical p-type semiconductors. Under normal conditions, for the p-type semiconductor, the valence band energy is about 0.1–0.2 eV (0.2 eV selected in this work), more positive than E_{fb}. Thus, the E_{VB} of $Bi_2O_3/Bi_2O_{2.33}$, and β-Bi_2O_3 are 2.00 eV and 1.69 eV, respectively. The conduction band energy can be calculated by Eq. (6):

$$E_{CB} = E_{VB} - E_g \quad (6)$$

where E_{CB}, E_{VB}, and E_g are conduction band energy, valence band energy and band gap of the semiconductor, respectively. Hence the E_{CB} of $Bi_2O_3/Bi_2O_{2.33}$ and β-Bi_2O_3 is − 0.93 eV and − 0.46 eV, respectively.

Trapping experiments were performed to detect the active species generated during photodegradation. TBA, EDTA-2Na, and BQ were used as scavengers to trap hydroxyl radicals (•OH), hole (h^+), and superoxide radicals ($\bullet O_2^-$). It can be observed from Fig. 6a, 6b and Fig. S8 that the photocatalytic degradation of RhB and TCH molecules is remarkably inhibited by adding EDTA-2Na and TBA. However, the addition of BQ does not cause significant deactivation of photocatalyst, illustrating that $\bullet O_2^-$ had little contribution to RhB and TCH photodegradation. These results demonstrate that h^+ and •OH are the main active species in the photocatalytic process under light irradiation.

EPR was employed to identify the active species in the photocatalytic process of the $Bi_2O_{2.33}/Bi_2O_3$. 5,5-dimethyl-lpyrroline N-oxide (DMPO) was employed as the spin-trapping agent. As shown in Fig. 6c, no DMPO-•OH signal is detected in the dark, while the characteristic 1:2:2:1 quadruple peaks of DMPO-•OH are observed under illumination, indicating the generation of hydroxyl radicals in the solution under light irradiation with $Bi_2O_{2.33}/Bi_2O_3$. As shown in Fig. 6d, no DMPO-$\bullet O_2^-$ signal is detected in the dark, while the characteristic peak of DMPO-$\bullet O_2^-$ is detected under illumination, indicating that the photogenerated electrons in $Bi_2O_{2.33}/Bi_2O_3$ reduces dissolved oxygen to generate

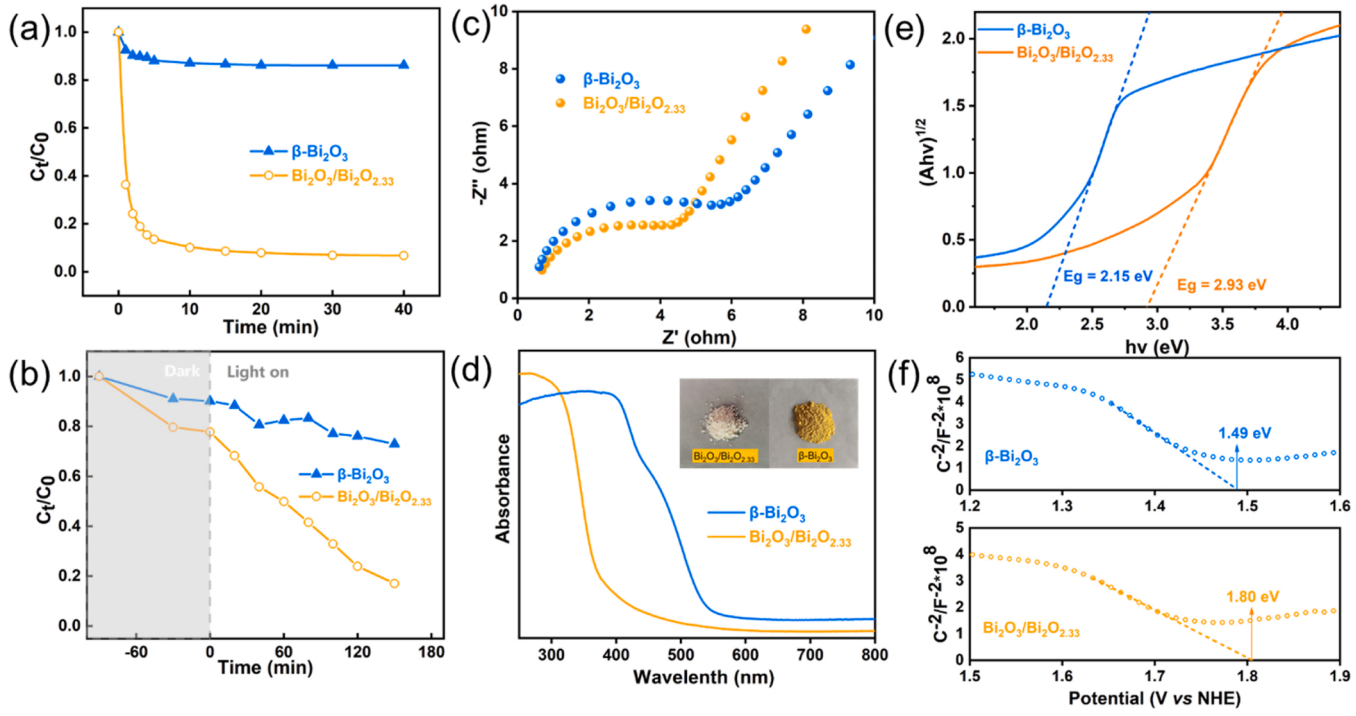

Fig. 5. (a) Adsorption kinetic curve of 100 mg L^{-1} MO solution with $Bi_2O_3/Bi_2O_{2.33}$ and β-Bi_2O_3, (b) Degradation curve of 10 mg L^{-1} RhB with $Bi_2O_3/Bi_2O_{2.33}$ and β-Bi_2O_3, (c) EIS spectra of $Bi_2O_3/Bi_2O_{2.33}$ and β-Bi_2O_3, (d) UV-vis diffuse reflectance spectra of $Bi_2O_3/Bi_2O_{2.33}$ and β-Bi_2O_3, (e) The plots of $(\alpha h\upsilon)^{1/2}$ and $(\alpha h\upsilon)^2$ vs. hυ, and (f) Mott-Schottky plots of $Bi_2O_3/Bi_2O_{2.33}$ and β-Bi_2O_3.

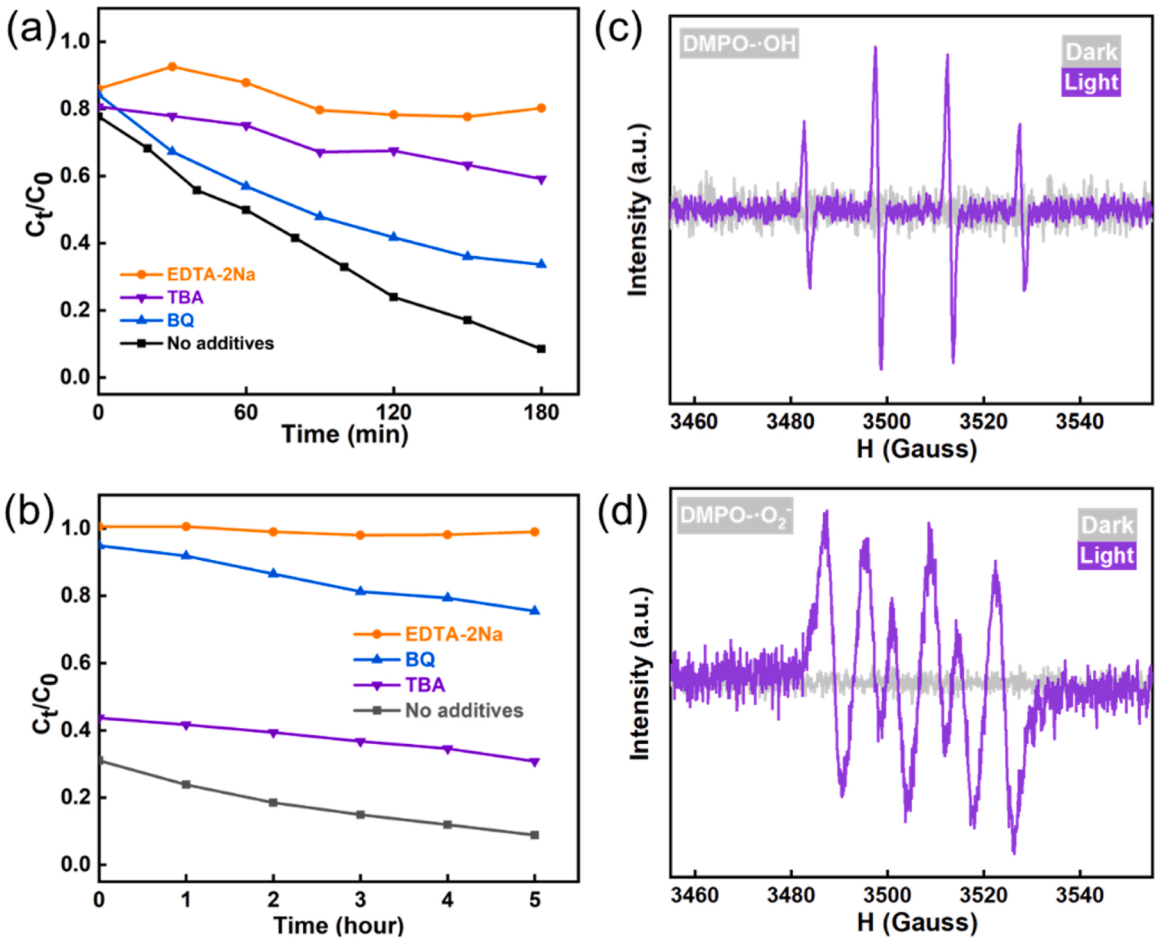

Fig. 6. Trapping experiments of active species over $Bi_2O_3/Bi_2O_{2.33}$ for photocatalytic degradation of (a) 10 mg L^{-1} RhB and (b) 50 mg L^{-1} TCH with addition of different scavengers. (c) DMPO-•OH and (d) DMPO-•O_2^- using $Bi_2O_3/Bi_2O_{2.33}$.

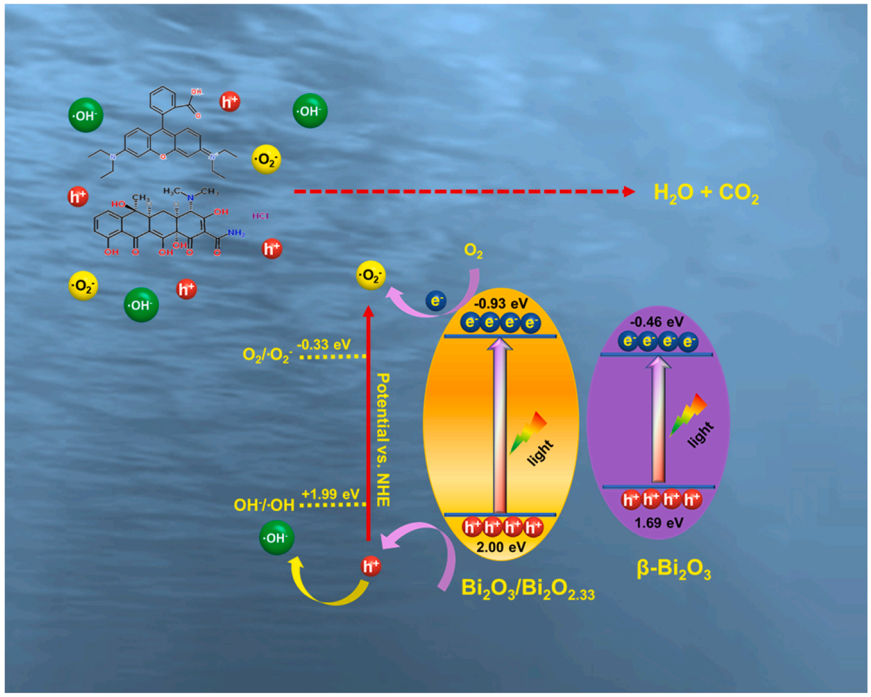

Fig. 7. Mechanism diagram of photocatalytic degradation by using $Bi_2O_3/Bi_2O_{2.33}$.

superoxide anion radicals. EPR analysis confirms the generation of •OH and $\bullet O_2^-$ during the photocatalytic process of the $Bi_2O_{2.33}/Bi_2O_3$.

Based on the above results, a plausible mechanism for $Bi_2O_3/Bi_2O_{2.33}$ to photodegrade RhB and TCH is proposed. The band structure of $Bi_2O_3/Bi_2O_{2.33}$ and standard redox potential ($OH^-/\bullet OH$, $O_2/\bullet O_2^-$) [20,45] are illustrated in Fig. 7. The degradation of contaminant molecules is mainly driven by the participation of h^+ and •OH radicals. When $Bi_2O_3/Bi_2O_{2.33}$ is irradiated by ultraviolet light, electrons and holes are generated in its CB and VB, respectively. Given that the $Bi_2O_3/Bi_2O_{2.33}$ CB potential (−0.93 eV vs. NHE) is more negative than the $O_2/\bullet O_2^-$ standard redox potential (−0.33 eV vs. NHE), the electrons in the $Bi_2O_3/Bi_2O_{2.33}$ CB are easily to reduce O_2 into $\bullet O_2^-$. On the other hand, the VB potential of $Bi_2O_3/Bi_2O_{2.33}$ (2.00 eV vs. NHE) is a little more positive than the $OH^-/\bullet OH$ (1.99 eV vs. NHE) standard redox potential, which means that the holes in the $Bi_2O_3/Bi_2O_{2.33}$ VB can oxidize OH^- into •OH to degrade organic pollutants. And the holes in the $Bi_2O_3/Bi_2O_{2.33}$ VB can be directly involved in the degradation of organic pollution. By comparison, the VB potential of β-Bi_2O_3 is not as positive as $Bi_2O_3/Bi_2O_{2.33}$ and its CB is also not as negative as $Bi_2O_3/Bi_2O_{2.33}$. Thus, the redox ability of photogenerated electrons and holes in β-Bi_2O_3 is weaker than that in $Bi_2O_3/Bi_2O_{2.33}$, causing its poor photodegradation performance.

4. Conclusion

A one-step hydrothermal method was used to synthesize $Bi_2O_{2.33}/Bi_2O_3$ and $Bi_2O_{2.33}/Bi_2O_3$@ECNF, exhibiting excellent adsorption and photocatalytic properties. $Bi_2O_3/Bi_2O_{2.33}$ exhibited favorable adsorption for anionic pollutant molecules with a high adsorption capacity of 213.13 mg g^{-1} for MO. $Bi_2O_{2.33}/Bi_2O_3$ effectively treated high concentrations of TCH through adsorption and degradation. The $Bi_2O_{2.33}/Bi_2O_3$ @ECNF was easily recyclable after removing organic pollutants and maintained good cycling stability. Therefore, this study provides a new, efficient, and convenient recycling solution for removing organic pollutants from water.

CRediT authorship contribution statement

Sheng-Zhe Zhao: Methodology, Writing – original draft. **Yi Yang:** Visualization. **Ran Lu:** Investigation. **Yan Wang:** Resources. **Yong-Da Hu:** Validation, Project administration. **Hong-Lan Huang:** Formal analysis. **Raul D. Rodriguez:** Writing – review & editing. **Jin-Ju Chen:** Conceptualization, Supervision.

Declaration of Competing Interest

The authors declare that they have no known competing financial interests or personal relationships that could have appeared to influence the work reported in this paper.

Data availability

The data that has been used is confidential.

Acknowledgements

The work was supported by the Sichuan Science and Technology Program (grant No 2023YFG0215). RDR thanks RFBR and DFG project number 21-53-12045.

Appendix A. Supporting information

Supplementary data associated with this article can be found in the online version at doi:10.1016/j.colsurfa.2023.131912.

References

[1] S.S. Liu, H.X. Zhao, H.J. Lehmler, X.Y. Cai, J.W. Chen, Antibiotic pollution in marine food webs in Laizhou Bay, North China: trophodynamics and human exposure implication, Environ. Sci. Technol. 51 (4) (2017) 2392–2400, https://doi.org/10.1021/acs.est.6b04556.
[2] A. Tkaczyk, K. Mitrowska, A. Posyniak, Synthetic organic dyes as contaminants of the aquatic environment and their implications for ecosystems: a review, Sci. Total Environ. 717 (2020), 137222, https://doi.org/10.1016/j.scitotenv.2020.137222.
[3] F.M.D. Chequer, G.A.R. de Oliveira, E.R.A. Ferraz, J.C. Cardoso, M.V.B. Zanoni, D. P. de Oliveira, Textile dyes: dyeing process and environmental impact, Eco Friendly Text. Dyeing Finish 6 (6) (2013) 151–176, https://doi.org/10.5772/53659.
[4] C. Manyi-Loh, S. Mamphweli, E. Meyer, A. Okoh, Antibiotic use in agriculture and its consequential resistance in environmental sources: potential public health implications, Molecules 23 (4) (2018) 795, https://doi.org/10.3390/molecules23040795.
[5] T.R. Das, S. Patra, R. Madhuri, P.K. Sharma, Bismuth oxide decorated graphene oxide nanocomposites synthesized via sonochemical assisted hydrothermal method for adsorption of cationic organic dyes, J. Colloid Interface Sci. 509 (2018) 82–93, https://doi.org/10.1016/j.jcis.2017.08.102.
[6] S. Senguttuvan, P. Senthilkumar, V. Janaki, S. Kamala-Kannan, Significance of conducting polyaniline based composites for the removal of dyes and heavy metals from aqueous solution and wastewaters-a review, Chemosphere 267 (2021), 129201, https://doi.org/10.1016/j.chemosphere.2020.129201.
[7] E. Felis, J. Kalka, A. Sochacki, K. Kowalska, S. Bajkacz, M. Harnisz, E. Korzeniewska, Antimicrobial pharmaceuticals in the aquatic environment-occurrence and environmental implications, Eur. J. Pharmacol. 866 (2020), 172813, https://doi.org/10.1016/j.ejphar.2019.172813.
[8] Y. Zhou, J. Lu, Y. Zhou, Y. Liu, Recent advances for dyes removal using novel adsorbents: a review, Environ. Pollut. 252 (2019) 352–365, https://doi.org/10.1016/j.envpol.2019.05.072.
[9] H. Huang, K. Xiao, T. Zhang, F. Dong, Y. Zhang, Rational design on 3D hierarchical bismuth oxyiodides via in situ self-template phase transformation and phase-junction construction for optimizing photocatalysis against diverse contaminants, Appl. Catal. B 203 (2017) 879–888, https://doi.org/10.1016/j.apcatb.2016.10.082.
[10] X. Liu, X. Duan, T. Bao, D. Hao, Z. Chen, W. Wei, D. Wang, S. Wang, B.J. Ni, High-performance photocatalytic decomposition of PFOA by BiOX/TiO_2 heterojunctions: self-induced inner electric fields and band alignment, J. Hazard. Mater. 430 (2022), 128195, https://doi.org/10.1016/j.jhazmat.2021.128195.
[11] Y. Zhong, C. Wu, Y. Feng, D. Chen, Y. Wang, D. Hao, H. Ding, Enriched surface oxygen vacancies of BiOCl boosting efficient charge separation, whole visible-light absorption, and photo to thermal conversion, Appl. Surf. Sci. 585 (2022), 152656, https://doi.org/10.1016/j.apsusc.2022.152656.
[12] S. Sayegh, M. Abid, F. Tanos, M. Cretin, G. Lesage, F. Zaviska, E. Petit, B. Navarra, I. Iatsunskyi, E. Coy, R. Viter, V. Fedorenko, A. Ramanavicius, A. Razzouk, J. Stephan, M. Bechelany, N-doped TiO_2 nanotubes synthesized by atomic layer deposition for acetaminophen degradation, Colloids Surf. A 655 (2022), 130213, https://doi.org/10.1016/j.colsurfa.2022.130213.
[13] G. Boczkaj, A. Fernandes, Wastewater treatment by means of advanced oxidation processes at basic pH conditions: a review, Chem. Eng. J. 320 (2017) 608–633, https://doi.org/10.1016/j.cej.2017.03.084.
[14] H. Zhao, X. Pang, Y. Huang, Y. Bai, J. Ding, H. Bai, W. Fan, Electrocatalytic reduction of 4-nitrophenol over Ni-MOF/NF: understanding the self-enrichment effect of H-bonds, Chem. Commun. 58 (31) (2022) 4897–4900, https://doi.org/10.1039/D2CC00111J.
[15] P.V. Nidheesh, M. Zhou, M.A. Oturan, An overview on the removal of synthetic dyes from water by electrochemical advanced oxidation processes, Chemosphere 197 (2018) 210–227, https://doi.org/10.1016/j.chemosphere.2017.12.195.
[16] K. Vikrant, B.S. Giri, N. Raza, K. Roy, K.H. Kim, B.N.R.S. Rai, Singh, Recent advancements in bioremediation of dye: current status and challenges, Bioresour. Technol. 253 (2018) 355–367, https://doi.org/10.1016/j.biortech.2018.01.029.
[17] M. Laqbaqbi, M.C. García-Payo, M. Khayet, J. El Kharraz, M. Chaouch, Application of direct contact membrane distillation for textile wastewater treatment and fouling study, Sep. Purif. Technol. 209 (2019) 815–825, https://doi.org/10.1016/j.seppur.2018.09.031.
[18] P.S. David, A. Karunanithi, N.N. Fathima, mproved filtration for dye removal using keratin–polyamide blend nanofibrous membranes, Environ. Sci. Pollut. Res. 27 (36) (2020) 45629–45638, https://doi.org/10.1007/s11356-020-10491-y.
[19] R. Yu, Y. Shi, D. Yang, Y. Liu, J. Qu, Z.Z. Yu, Graphene oxide/chitosan aerogel microspheres with honeycomb-cobweb and radially oriented microchannel structures for broad-spectrum and rapid adsorption of water contaminants, ACS Appl. Mater. Interfaces 9 (26) (2017) 21809–21819, https://doi.org/10.1021/acsami.7b04655.
[20] C. Tian, H. Zhao, H. Sun, K. Xiao, P.K. Wong, Enhanced adsorption and photocatalytic activities of ultrathin graphitic carbon nitride nanosheets: kinetics and mechanism, Chem. Eng. J. 381 (2020), 122760, https://doi.org/10.1016/j.cej.2019.122760.
[21] Q. Zhang, Z. Zhu, X. Zhao, X. Xiao, X. Zuo, J. Nan, Efficient and effective removal of emerging contaminants through the parallel coupling of rapid adsorption and photocatalytic degradation: a case study of fluoroquinolones, Chemosphere 280 (2021), 130770, https://doi.org/10.1016/j.chemosphere.2021.130770.
[22] S. Natarajan, H.C. Bajaj, R.J. Tayade, Recent advances based on the synergetic effect of adsorption for removal of dyes from waste water using photocatalytic process, J. Environ. Sci. 65 (2018) 201–222, https://doi.org/10.1016/j.jes.2017.03.011.

[23] H. Wang, X. Yuan, Y. Wu, G. Zeng, H. Dong, X. Chen, L.J. Leng, Z.B. Wu, L. Peng, In situ synthesis of In_2S_3@ MIL-125 (Ti) core-shell microparticle for the removal of tetracycline from wastewater by integrated adsorption and visible-light-driven photocatalysis, Appl. Catal., B 186 (2016) 19–29, https://doi.org/10.1016/j.apcatb.2015.12.041.

[24] Y. Su, S. Li, G. Jiang, Z. Zheng, C. Wang, S. Zhao, D. Cui, Y. Liu, B. Zhang, Z. Zhang, Synergic removal of tetracycline using hydrophilic three-dimensional nitrogen-doped porous carbon embedded with copper oxide nanoparticles by coupling adsorption and photocatalytic oxidation processes, J. Colloid Interface Sci. 581 (2021) 350–361, https://doi.org/10.1016/j.jcis.2020.07.071.

[25] J. Cao, Z.H. Yang, W.P. Xiong, Y.Y. Zhou, Y.R. Peng, X. Li, C.Y. Zhou, R. Xu, Y. R. Zhang, One-step synthesis of Co-doped UiO-66 nanoparticle with enhanced removal efficiency of tetracycline: simultaneous adsorption and photocatalysis, Chem. Eng. J. 353 (2018) 126–137, https://doi.org/10.1016/j.cej.2018.07.060.

[26] A. Safri, A.J. Fletcher, Effective carbon/TiO_2 gel for enhanced adsorption and demonstrable visible light driven photocatalytic performance, Gels 8 (4) (2022) 215, https://doi.org/10.3390/gels8040215.

[27] G. Chandrabose, A. Dey, S.S. Gaur, S. Pitchaimuthu, H. Jagadeesan, N.S. J. Braithwaite, V. Selvaraj, V. Kumar, S. Krishnamurthy, Removal and degradation of mixed dye pollutants by integrated adsorption-photocatalysis technique using 2-D MoS_2/TiO_2 nanocomposite, Chemosphere 279 (2021), 130467, https://doi.org/10.1016/j.chemosphere.2021.130467.

[28] J. Niu, Y. Xie, H. Luo, Q. Wang, Y. Zhang, Y. Wang, Cobalt oxide loaded graphitic carbon nitride as adsorptive photocatalyst for tetracycline removal from aqueous solution, Chemosphere 218 (2019) 169–178, https://doi.org/10.1016/j.chemosphere.2018.11.111.

[29] J. Lyu, Z. Hu, Z. Li, M. Ge, Removal of tetracycline by BiOBr microspheres with oxygen vacancies: combination of adsorption and photocatalysis, J. Phys. Chem. Solids 129 (2019) 61–70, https://doi.org/10.1016/j.jpcs.2018.12.041.

[30] S. Huang, G. Wang, J. Liu, C. Du, Y. Su, A novel $CuBi_2O_4$/BiOBr direct Z-scheme photocatalyst for efficient antibiotics removal: synergy of adsorption and photocatalysis on degradation kinetics and mechanism insight, ChemCatChem 12 (17) (2020) 4431–4445, https://doi.org/10.1002/cctc.202000634.

[31] Q. Huang, S. Zhang, C. Cai, B. Zhou, β-and α-Bi_2O_3 nanoparticles synthesized via microwave-assisted method and their photocatalytic activity towards the degradation of rhodamine B, Mater. Lett. 65 (6) (2011) 988–990, https://doi.org/10.1016/j.matlet.2010.12.055.

[32] J. Dai, X. Chen, H. Yang, Visible light photocatalytic degradation of dyes by a new polyaniline/β-Bi_2O_3 composite, Inorg. Nano Met. Chem. 47 (9) (2017) 1364–1368, https://doi.org/10.1080/24701556.2017.1284128.

[33] S. Liu, S. Kang, H. Wang, G. Wang, H. Zhao, W. Cai, Nanosheets-built flowerlike micro/nanostructured $Bi_2O_{2.33}$ and its highly efficient iodine removal performances, Chem. Eng. J. 289 (2016) 219–230, https://doi.org/10.1016/j.cej.2015.12.101.

[34] M. Schuisky, A. Hårsta, Epitaxial growth of $Bi_2O_{2.33}$ by halide Cvd, Chem. Vap. Depos. 2 (6) (1996) 235–238, https://doi.org/10.1002/cvde.19960020604.

[35] Y. Bian, Y. Ma, Y. Shang, P. Tan, J. Pan. Self-integrated β-Bi_2O_3/$Bi_2O_{2.33}$@ $Bi_2O_2CO_3$ ternary composites: formation mechanism and visible light photocatalytic activity, Appl. Surf. Sci. 430 (2018) 613–624, https://doi.org/10.1016/j.apsusc.2017.06.063.

[36] J. Chen, J. Wang, Y. Peng, F. Liu, M. Jia, Y. Lai, J. Li, L. Jiang, $Bi_2O_{2.33}$ nanostructure-based photoanodes for photoelectrochemical determination of trace soluble sulfides, ACS Appl. Nano Mater. 4 (6) (2021) 5778–5784, https://doi.org/10.1021/acsanm.1c00592.

[37] Y. Peng, K.K. Wang, T. Liu, J. Xu, B.G. Xu, Synthesis of one-dimensional Bi_2O_3-$Bi_2O_{2.33}$ heterojunctions with high interface quality for enhanced visible light photocatalysis in degradation of high-concentration phenol and MO dyes, Appl. Catal. B 203 (2017) 946–954, https://doi.org/10.1016/j.apcatb.2016.11.011.

[38] H. Guan, X. Zhang, Y. Xie, Soft-chemical synthetic nonstoichiometric $Bi_2O_{2.33}$ nanoflower: a new room-temperature ferromagnetic semiconductor, J. Phys. Chem. C 118 (46) (2014) 27170–27174, https://doi.org/10.1021/jp509045d.

[39] H. Bai, F. Wang, Q. Ding, W. Xie, H. Li, G. Zheng, W. Fan, Construction of frustrated Lewis pair sites in CeO_2–C/$BiVO_4$ for photoelectrochemical nitrate reduction, Inorg. Chem. 62 (5) (2023) 2394–2403, https://doi.org/10.1021/acs.inorgchem.2c04208.

[40] X. Pang, H. Bai, Y. Huang, H. Zhao, G. Zheng, W. Fan, Mechanistic insights for dual-species evolution toward 5-hydroxymethylfurfural oxidation, J. Catal. 417 (2023) 22–34, https://doi.org/10.1016/j.jcat.2022.11.029.

[41] X. Pang, H. Bai, H. Zhao, W. Fan, W. Shi, Efficient electrocatalytic oxidation of 5-hydroxymethylfurfural coupled with 4-nitrophenol hydrogenation in a water system, ACS Catal. 12 (2) (2022) 1545–1557, https://doi.org/10.1021/acscatal.1c04880.

[42] Z. Xiao, Y.C. Huang, C.L. Dong, C. Xie, Z. Liu, S. Du, W. Chen, D. Yan, L. Tao, Z. Shu, H. Duan, Y. Wang, Y. Zou, R. Chen, S. Wang, Operando identification of the dynamic behavior of oxygen vacancy-rich Co_3O_4 for oxygen evolution reaction, J. Am. Chem. Soc. 142 (28) (2020) 12087–12095, https://doi.org/10.1021/jacs.0c00257.

[43] B. Liu, C. Li, G. Zhang, X. Yao, S.S. Chuang, Z. Li, Oxygen vacancy promoting dimethyl carbonate synthesis from CO_2 and methanol over Zr-doped CeO_2 nanorods, ACS Catal. 8 (11) (2018) 10446–10456, https://doi.org/10.1021/acscatal.8b00415.

[44] D.A. Yaseen, M. Scholz, Textile dye wastewater characteristics and constituents of synthetic effluents: a critical review, Int. J. Environ. Sci. Technol. 16 (2) (2019) 1193–1226, https://doi.org/10.1007/s13762-018-2130-z.

[45] Y. Wang, S. Zhao, Y. Yang, R.D. Rodriguez, A. Lipovka, Y. Lu, H. Huang, J. Chen, Ag nanoparticle-decorated Bi_2O_3-TiO_2 heterogeneous nanotubular photocatalysts for enhanced degradation of organic contaminants, Colloids Surf. A 648 (2022), 129233, https://doi.org/10.1016/j.colsurfa.2022.129233.